Bifunctional Praseodymium-doped SnS_2 thin films for photocatalytic and antibacterial applications

Abdelkader Nebatti Ech-Chergui[1]*, Farid Bennabi[1], Mehmet Isik[2], Yasmina Khane[3], Francisco José García García[4], Ali Sadek Kadari[6], M'hamed Guezzoul[5], Ashmalina Rahman[7], Mohammad Mansoob Khan[7]*, Adjdir Mehdi[8], Kouider Driss-Khodja[6] ,Bouhalouane Amrani[6]

[1]Laboratory of Applied Hydrology and Environment, University Belhadj Bouchaib, Ain-Temouchent, Algeria

[2]Department of Electrical and Electronics Engineering, Atilim University, 06836 Ankara, Turkey.

[3]Faculty of science and technology, University of Ghardaia, BP455, 47000, Ghardaia, Algeria.

[4]Dpto. Ingeniería y Ciencia de los Materiales y del Transporte, Escuela Técnica Superior de Ingeniería, Universidad de Sevilla, Camino de los Descubrimientos, 41092 Seville, Spain.

[5]Laboratory of materials (LABMAT), National Polytechnique School (ENP) of Oran, BP1523 Oran Mnaouar, Oran, Algeria.

[6]Laboratory of Theory and Simulation of Materials, Faculty of Exact and Applied Sciences, University of Oran1 Ahmed Ben Bella, Oran, Algeria.

[7]Chemical Sciences, Faculty of Science, Universiti Brunei Darussalam, Jalan Tungku Link, Gadong, BE 1410, Brunei Darussalam.

[8]Applied Organic Synthesis Laboratory, Department of Chemistry, Faculty of Science, University of Oran, BP 1524, El Menaouar Oran, 31000, Algeria.

Published by COLLOIDS AND SURFACES A-PHYSICOCHEMICAL AND ENGINEERING ASPECTS

https://doi.org/10.1016/j.colsurfa.2024.133362

Abstract

This paper introduces a novel application of bifunctional Pr-doped SnS_2 thin films, demonstrating their efficacy in both photocatalytic degradation of dye and antibacterial activities. The thin films were fabricated using an eco-friendly spray-coated method, encompassing undoped and Pr-doped SnS_2 variations. The study comprehensively examines the structural, morphological, chemical, photocatalytic, and antibacterial characteristics of these films. The crystal structure of both undoped and Pr-doped SnS_2 thin films exhibited hexagonal patterns, prominently favouring the growth in (1 0 1) orientation. Notably, an increase in crystallite size was observed with higher levels of Pr-doping. Raman spectroscopy analysis highlighted a distinct peak at 315 cm^{-1}, corresponding to the A_{1g} vibrational mode associated with Sn-S bonds along the c-axis of the structure. Employing X-ray Photoelectron Spectroscopy (XPS), the presence of essential components – Sn, S, and Pr – within the fabricated thin films

was confirmed, consistent with experimental values of undoped and Pr-doped SnS_2-x compositions. Importantly, the XPS analysis confirmed the integration of the Pr^{3+} oxidation state within Pr-doped SnS_2 films. The photocatalytic degradation and antibacterial activities of the films were investigated. Notably, the photocatalytic potential of the synthesized materials against Congo Red exhibited a direct correlation with the Pr^{3+} doping percentage, indicating enhanced pollutant degradation with increasing doping levels. Similarly, the antibacterial performance against *Escherichia coli* displayed improvement with increasing Pr-doping content, highlighting the promising antimicrobial capabilities of the films. This study presents an innovative avenue to address both organic pollutant degradation and microbial control. By harnessing the attributes of Pr-doped SnS_2 thin films, this research introduces a promising strategy for sustainable material applications in environmental purification and improvement in public health.

Keywords: Tin sulfide; SnS_2; Pr-doped SnS_2; Photocatalysis; Photocatalysts; Antibacterial studies

1. Introduction

Heavy metals, dyes, and pesticides are three potential contributors to water pollution [1]. The majority of wastewater pollution is caused by organic dyes, which are utilized in the leather, textile, pulp, cosmetic, and pharmaceutical industries. There is a risk that these dyes will harm the living things on the Earth [2,3]. However, these persistent organic pollutants are made up of carbon-based chemical substances that are challenging to degrade in their natural state and that may not be entirely removed by the biological, physical, and chemical processes that are typically used. To get rid of pollutants entirely requires a lot of energy and results in the production of hazardous secondary pollutants such as toxic sludge, heavy metals, and solid waste. This is because pollutants are stable when exposed to oxidants [4,5].

Researchers have focused on finding new energy sources to address environmental pollution and energy depletion. Multi-phase semiconductors are promising for photocatalytic and electrocatalytic hydrogen production from water [6,7] and photocatalytic water chemical elimination [8]. In photocatalysis, semiconductors like zinc sulfide (ZnS) [9,10], tin sulfide (SnS_2) [11,12], copper sulfide (CuS) [13,14], zinc oxide (ZnO) [15,16], and titanium dioxide (TiO_2) [17,18] are a few examples of the numerous semiconductors that are utilized in the field of photocatalysis. Due to the chemical stability, low cost, and non-toxic characteristics of chalcogenides, are narrow-band gap semiconductors are commonly employed as photocatalysts [19,20]. These narrow-band gap materials absorb approximately 40% of visible solar energy,

improving photocatalytic capabilities. These compounds provide e−/h+ pairs when exposed to visible light [21–23]. Photo-generated e−/h+ couples have been used to split water into hydrogen and oxygen to remove and degrade environmental industrial, pharmaceutical, and agricultural organic/inorganic/biological contaminants [24]. Among these chalcogenides, tin sulfide (SnS_2) is a semiconductor that can be characterized as a CdI_2-type layered non-noble metal sulfide [25]. It exhibits an n-type direct band gap energy (ranging from 2.19 to 2.41 eV) and possesses properties of harmlessness and relative inexpensiveness [26]. Gedi *et al.* presented a comprehensive review of tin-based binary sulfides (Sn_xS_y) synthesized through a solution process [27]. The review underscored the significance of comprehending deposition parameters to enhance film quality and device performance, particularly in the realms of photovoltaics, photocatalysis, and thermoelectrics. SnS_2 has demonstrated great potential as a photocatalyst under visible light and short-wavelength near-infrared irradiation, primarily due to its narrow band gap. However, its poor photoinduced electrons and holes separation restricts its photocatalytic efficiency.

Numerous attempts have been made to overcome these problems. For instance, Guo *et al.* have reported that one effective approach to enhancing the performance of SnS_2 in various photocatalytic applications involves the construction of SnS_2 composites [25]. Non-metallic doping, as they suggest, can further enhance the S Scheme heterojunction, thereby accelerating the process of charge separation. Moreover, Goktas and co-workers have fabricated $Sn_{1-x}Zn_xS$ (x = 0.00–0.20) nanostructured thin films via a solution process for optoelectronic, photocatalytic, and gas-sensing applications [28]. These films demonstrated improved properties compared to pure SnS, with the $Sn_{0.99}Zn_{0.01}S$ film exhibiting high photocatalytic efficiency under sunlight. The results highlight the promise of Zn-substituted SnS thin films for various applications, including photocatalysis and optoelectronics. Moreover, Gadore *et al.* pioneered eco-friendly wastewater treatment using SnS_2-biochar, showing potent pollutant removal with real-world relevance [29]. Among them, doping has been reported to be one of the effective methods to modify the properties of SnS_2 and eventually improve its photocatalytic activity [30]. In another study, Prabha *et al*. reported an improved magnetic attraction, enhanced light penetration, and increased antibacterial properties were also observed when Sr was introduced into SnS_2 [31]. Additionally, Yang *et al*. reported the enhanced SnS_2 by incorporating Ag for efficient sunlight-driven removal of uranium in water [32]. In another study, Diko *et al.* have explored SnS_2-carbon composites for energy-saving and sunlight-driven cleansing applications [33]. Similarly, Ech-Chergui *et al.* have synthesized La-doped 2D-SnS_2

films for potential use in photocatalytic degradation [34]. Films with 2% and 4% La doping exhibited structural changes, increased hardness, and a widened bandgap. Notably, the photocatalytic efficiency improved with La doping, reaching 62.92% for 4% La-doped SnS_2. These findings collectively reveal the evolving potential of SnS_2-based materials and their diversified applications for betterment.

Doping of appropriate various elements with proper concentration in SnS_2 is an excellent way to improve its properties for photocatalytic activity. Among the different dopants reported, praseodymium (Pr) was chosen because of its unique interband 4f–5d and intraband 4f–4f electronic transitions. The incorporation of Pr as an impurity results in lattice deformation in SnS_2 and may create a mid-gap state within the band structure of SnS_2 tuning its optical band gap energy and extending the light absorption range. As a consequence, it can also hinder the recombination of electron-hole pairs when exposed to light. In addition, Pr can be successfully doped into SnS_2 [35,36]. Recently, research led by Zhang and co-workers has utilized a two-step hydrothermal method to fabricate 3D nanoflowers composed of SnS_2/ZnS with Pr doping for gas sensing [37].

This study introduces a pioneering approach to the fabrication of SnS_2 and Pr-doped SnS_2 through the utilization of a spray coating procedure, marking the first instance of such synthesis. This method is cost-effective, easy to use, and allows for quick application. Using clear molecular ink adds something new to the process, making sure the film is spread evenly and consistently. This also helps to control the thickness and composition of the films. Additionally, an in-depth exploration into the influence of Pr doping on the structural and morphological attributes of the resultant SnS_2 was conducted. Notably, there are no previous studies that have been explored on the utilization of Pr-doped SnS_2 for photocatalytic and antibacterial purposes. In this study, novel investigations encompassed the evaluation of photocatalytic and antibacterial potentials of the synthesized SnS_2 and Pr-doped SnS_2 thin films under both visible light conditions and in their absence were carried out, offering unprecedented insights into their functionalities.

2. Methodology

2.1. Starting materials/Chemicals used

All of the chemicals used in this experiment were purchased from Sigma Aldrich and utilized in their unpurified forms without undergoing any additional processing which includes tin chloride ($SnCl_2 \cdot 2H_2O$), thiourea ($SC(NH_2)_2$), praseodymium chloride ($PrCl_2 \cdot 2H_2O$). Methanol, Congo red (CR), Mueller-Hinton nutrient agar, and broth were obtained from

Biochem Chemopharma, France. The gram-negative bacterial strain, *E. coli* (ATCC 25922) was obtained from Algeria, at Ain Temouchent University's Microbiology laboratory and the distilled water was supplied from the chemical laboratory.

2.2. Synthesis of SnS_2 and Pr-doped SnS_2

Syringe pump spray coating was used to fabricate undoped and Pr-doped SnS_2 thin films on glass substrates using a spray pyrolysis machine (Model No. HO-TH-04, Holmarc Ltd., India), as previously described [38–40]. Substrates with a measurement of 20 mm x 10 mm were cut from glass slides. After being cured in acetone, the substrates were cleaned ultrasonically, rinsed in deionized water, and dried using an air jet. Next, the cleaned glass substrates were placed on a hot plate and heated to 100 °C in 20 °C increments to remove the remaining solvent. The deposition of the undoped, 2% Pr-doped SnS_2, and 4% Pr-doped SnS_2 was carried out under the same conditions. The film's precursor undergoes when heated to thermolysis temperature (annealing temperature). To make the precursor solution, methanol was mixed with 0.05 mM $SnCl_2{\cdot}2H_2O$ and 0.1 mM $SC(NH_2)_2$. A component of 1 mL HCl was added to stop $SnCl_2$ from being hydrolyzed. The final solution was preloaded in a glass syringe pump with a 20 mL internal volume and sprayed through a spray nozzle with a set inner diameter of 0.2 mm. By regulating the pressure of the airflow, the desired droplet sizes may be produced. There was a 13 cm gap between the syringe and the substrate holder. At a constant air pressure of 1 bar and a dispensing spray rate of 500 μL/min, spraying through the syringe yielded tiny droplets in under 3 min. The thin films were sprayed at 100 °C forming a thin film of liquid. Then, they were subjected to a 30 min annealing process in air at 280 °C in order to undergo a thermochemical conversion to a solid film. To further explore the doping effect on the physical properties of the produced thin films, a different amount of $PrCl_2{\cdot}2H_2O$ was dissolved in the precursor solution for the Pr atomic concentrations of 2 and 4 at. %.

2.3 Characterizations of SnS_2 and Pr-doped SnS_2

The surface morphology and particle size of undoped SnS_2 and Pr-doped SnS_2 were determined using Field emission scanning electron microscopy (FE-SEM, Model, Country). The formation and phase purity of SnS_2 and different atomic percentages of Pr-doped SnS_2 were determined using powder X-ray diffraction analysis (XRD, Rigaku Miniflex diffractometer, Cu-Kα, λ = 1.54Å, radiation source). The Raman spectra were obtained from a Raman spectrometer (Horiba Jobin Yvon RMS-550) supplied with a 532 nm line of YAG:Nd^{3+} laser in the wavelength range of 200–800 cm^{-1}. X-ray photoelectron spectroscopy analysis (XPS) was performed using a Specs Phoibos 150 MCD instrument. The spectra were recorded at the Al-

Kα excitation line energy (hν=1486.6 eV). The XPS data were processed using CasaXPS software to identify photoelectron peaks associated with various elements. Additionally, CasaXPS was employed to calculate the atomic percentages of various elements, taking into account the corresponding relative sensitivity factors (RSF). The binding energies of the XPS spectra were calibrated using the C 1s line energy (284.8 eV) corresponding to the adventitious carbon. UV–visible spectral analysis was carried out using a specord 210 plus model spectrophotometer and was used to monitor the decrease in absorbance of the CR dye in the range of 200-800 nm.

2.4 Photocatalytic degradation of Congo red

CR aqueous solution was used as an organic pollutant for the measurement of photo-catalytic degradation of SnS_2 synthesized at different temperature and different thin film of Pr-doped SnS_2 materials under visible light irradiation at room temperature and pH = 6.8 [41]. At the beginning, the experiments into photocatalysis were carried out using a batch system. Each undoped SnS_2 and the Pr-doped SnS_2 thin film was incubated in 50 mL CR solution (10 mg/L) in the dark (to prevent any degradation from taking place because the visible light) for 30 min in order to reach the adsorption/desorption equilibrium before subjecting them to visible light irradiation. After that, the dye was exposed to visible light irradiation from a Philips LED lamp with a 40 W energy output so that the photocatalytic degradation process could begin. Using a UV-visible spectrophotometer, an estimate of the absorbance was made after passing varying amounts of time at the maximum wavelength of the dye, which was 490 nm. The percentage of photocatalytic degradation of CR was calculated using equation (1):

$$\text{Degradation } (\%) = \frac{C_0 - C_t}{C_0} \times 100 \ldots\ldots\ldots\ldots\ldots\ldots\ldots\ldots\ldots\ldots (1)$$

where, C_0 and C_t the initial concentration and the concentration of CR after incubation with thin film and visible light irradiation, respectively.

2.5. Photocatalytic antibacterial studies

Escherichia coli (*E. coli*, ATCC 25922), a pathogenic gram-negative bacterium was used as the test microorganism for the time-kill method to assess the antibacterial activity of the SnS_2 and Pr-doped SnS_2 thin films [42]. In this work, overnight cultures of the *E. coli* strains employed were diluted to 1:100 using Mueller-Hinton broth medium and then cultivated at 37 °C for 18 h to an optical density of 0.1 at 600 nm with a final cell density of 6 log colony forming units (CFU)/mL using 100 mL of the appropriate media. As previously reported by Kim *et al.* [42]. After being autoclaved at 120 °C for 30 min to sanitize all glass samples, all

obtained film was submerged in flasks containing 10 mL of a microbiological suspension with 106 CFU/mL [43,44] and one containing 10 mL of a microbiological suspension without any thin film was used as a negative control. The flasks were incubated at 37 °C for 24 h while being exposed to visible light [44]. Subsequently, 10 mL of the microbial cells from each flask were removed at different time intervals (0, 6, 12, and 24 h) and suspended in 10 mL of the broth solution for incubation at 37 °C for 24 h [45]. After three replicates, the percentage of dead cells was calculated relative to the number of growth colonies at t = 0 by counting the number of living cells (CFU/mL) and determining the optical density of each flask using a UV-vis spectrophotometer at = 610 nm.

3. Results and discussion

3.1 X-ray diffraction of SnS_2 and Pr-doped SnS_2

The XRD patterns depicted in **Figure 1(a)** illustrate the characteristics of undoped SnS_2 and various atomic percentages of Pr-doped SnS_2. The discernible diffraction peaks observed at 14.95° and 31.90° in the synthesized materials can be ascribed to the (001) and (101) crystallographic planes of the hexagonal phase of SnS_2 [46] (JPCDS No. 00-023-0677). In a recent investigation focusing on the impact of the starting precursor, Aslan *et al.* reported analogous findings when utilizing tin (II) chloride dihydrate [47]. On the other hand, numerous studies have consistently highlighted the prevalence of the (001) plane in SnS_2 when employing the spray pyrolysis technique [48–51]. Within the context of this study, the intensification of the (101) plane peak with increasing Pr doping signifies the escalating predominance of the (101) preferred orientation within the hexagonal SnS_2 structure. It is well-established that an augmentation in the intensity of a particular plane correlates with an enhancement in the monocrystalline of the material [52]. Consequently, the introduction of Pr doping serves to increase the crystallinity of the hexagonal phase of SnS_2, specifically favoring the (101) orientation. This observation underscores the influence of Pr doping on the structural characteristics of SnS_2, pointing towards an improvement in crystalline order with a pronounced preference for the (101) crystallographic orientation.

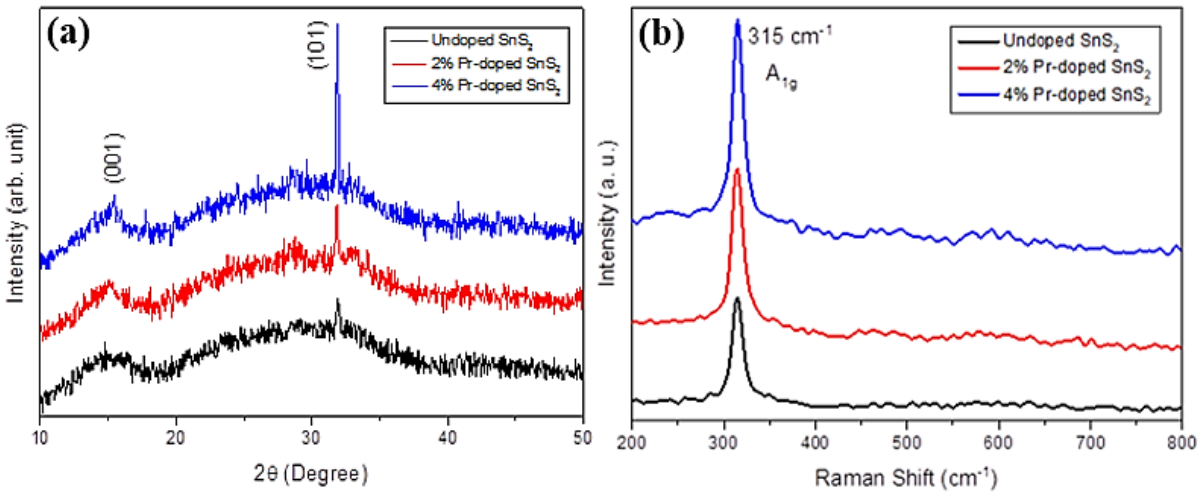

Figure 1. (a) XRD patterns and **(b)** Raman spectra of SnS_2, 2% Pr-doped SnS_2 and 4% Pr-doped SnS_2 thin films**.**

To gain deeper insights, the lattice parameters (a, c, and c/a), crystallite size, strain, and dislocation density for the three films are summarized in **Table 1**. The lattice constant "a" shows a slight increase with Pr doping, whereas the lattice constant "c" exhibits a contrary trend. Interestingly, the c/a ratio consistently decreases with rising Pr doping, even though the ionic radii of the dopant Pr^{3+} (1.13 Å) are larger than those of the host Sn^{4+} (0.69 Å). The above findings discerned alterations suggest an expansion of the crystal lattice specifically along the basal plane, concomitant with a distinctive impact along the vertical axis, induced by the specific interaction of Pr dopants with the crystal lattice. Furthermore, the steady decrease in the aspect ratio intimates a potential preferential influence of Pr doping on the crystal structure, potentially shaping the anisotropic characteristics of the material. Notably, the observed c/a ratio falling below the ideal value $\left(c/a=\sqrt{8/3}=1.633\right)$ strongly indicates stress within the films [53]. Moreover, the intricate interplay of lattice mismatch and distinct thermal extinction coefficients between the film and substrate emerges as influential factors shaping the lattice parameters [54]. These external influences contribute to the nuanced shifts observed in the crystal lattice.

Crystallite size is considered a gauge of the dimensions of coherently diffracting domains [55]. Owing to the formation of polycrystalline aggregates, it's important to note that the crystallite size of particles differs from the particle size. The average crystallite size of the SnS2 thin films is determined using the Debye-Scherrer formula [56]:

$$D=\frac{0.9\cdot\lambda}{\beta\cdot\mathrm{Cos}\theta}\ \ldots\ldots\ldots\ldots\ldots\ldots\ldots\ldots\ldots\ldots\ldots\ldots\ldots\ldots\ldots\ldots\ldots\ (2)$$

where λ is the wavelength of Cu-Kα radiation, θ is Bragg's angle and β is full width at half maxima (FWHM) of diffraction peak. It was observed that upon increasing the Pr content, the crystallite size increases. The average crystallite sizes were found to be 29.08, 59.40, and 65.03 nm for undoped SnS_2, 2% Pr-doped SnS_2, and 4% Pr-doped SnS_2, respectively.

Table 1. The calculated lattice constants, crystallite size, lattice strain, and dislocation density of SnS_2, 2% Pr-doped SnS_2 and 4% Pr-doped SnS_2 thin films.

Sample	Lattice constants (Å)			Crystallite size	Strain	Dislocation density
	a	c	c/a	(nm)	(ε) (× 10^{-4})	(δ) (× 10^{-3} line/m^2)
Undoped SnS_2	3.610	5.911	1.637	29.08	11.9	1.18
2% Pr-doped SnS_2	3.629	5.883	1.621	59.40	5.83	0.28
4% Pr-doped SnS_2	3.639	5.884	1.616	65.03	5.32	0.23

The relations (3) and (4) has been used to estimate the lattice strain and dislocation density [57]:

$$\varepsilon = \frac{\beta \cdot \mathrm{Cos}\,\theta}{4} \quad \ldots (3)$$

$$\delta = \frac{1}{D^2} \quad \ldots (4)$$

It is clearly shown in **Table 1** that both the micro-strain (ε) and the dislocation density (δ) decrease with an increase in Pr doping up to 4 at%, which leads to the carriers moving freely in the lattice. The strain values of SnS_2 decreased from 11.9 to 5.83 and 5.32 × 10^{-4} and the dislocation density decreased from 1.18 to 0.23 × 10^{-3} line/m^2 as Pr-doping increased to 4%. It was consistently observed that both micro-strain and dislocation density in the film decreases as the crystallite size increases, a phenomenon well-established [58]. This trend may arise from a variety of internal and external factors, including the exchange of ions with different ionic radii, lattice constant mismatch, the emergence of impurities/defects, and the thermal extinction coefficient difference between the substrate and the film [54,59]. Based on these results, it shows that Pr doping could result in enhancement in the crystal defects and lattice distortion as verified by the ε and δ values [28].

In summary, the XRD findings collectively signify a complex interplay between Pr dopants and the SnS_2 crystal lattice. A more profound comprehension of the underlying mechanisms steering these changes can be gleaned through meticulous analysis, encompassing detailed crystallographic studies or computational simulations. Such endeavors promise to unveil the intricate dynamics governing the structural evolution induced by Pr doping in hexagonal SnS_2.

3.2. Raman analysis of SnS_2 and Pr-doped SnS_2

The Raman spectra of undoped SnS_2, 2% Pr-doped SnS_2, and 4% Pr-doped SnS_2 thin films are shown in **Figure 1(b)**. The recorded spectra for all synthesized thin films exhibited a strong peak around 315 cm^{-1} which is related to the characteristic active mode of A_{1g}. This vibrational mode of SnS_2 corresponds to the symmetric stretching of S and Sn atoms along the c-axis of the crystal lattice [60]. This infrared active mode has been extensively studied by experimental and theoretical techniques like Raman and infrared spectroscopy [61], first principal calculations [60], and density functional theory simulations [62]. As sown in **Figure 1(b)**, when the Raman spectra of the synthesized thin films are compared, it is seen that the Raman intensity increases as the doping concentration increases. Upon comparing the Raman spectra of the synthesized thin films, a noticeable trend emerges wherein the Raman intensity rises with increasing doping concentration. This escalation in Raman intensity is frequently linked to enhanced crystallinity, resulting in more pronounced and distinct Raman peaks. This observation aligns well with the findings from XRD, reinforcing the correlation between improved crystallinity and heightened Raman signals. Similar behavior has been documented in various studies within the existing literature[57,63]. This can be shown as evidence that the Pr-atoms have been substituted in the SnS_2 host lattice.

3.3. SEM and EDS mapping of Pr-doped SnS_2 films

Figure 2(a) depicts the SEM image of 4% Pr-doped SnS_2 with grain-like spherical morphology. The film thickness is estimated from the cross-sectional SEM **figure (2b)** and it is not dependent on the concentration of Pr. The film thickness is approximately 1.2 μm. The EDS data is tabulated **in Figure 2(c)** which reveals that the 4% Pr-doped SnS_2 is composed of Sn and S with an atomic ratio of approximately 1:2 which is equal to the theoretical stoichiometric ratio in SnS_2. Based on the EDS results, also confirmed the presence of only Sn, S, and Pr in the synthesized Pr-doped SnS_2 as no other impurities were observed. **Figure 2 (d−f)** shows EDS elemental mapping of 4% Pr-doped SnS_2 which further confirms the presence of Sn, S, and Pr in the synthesized Pr-doped SnS_2.

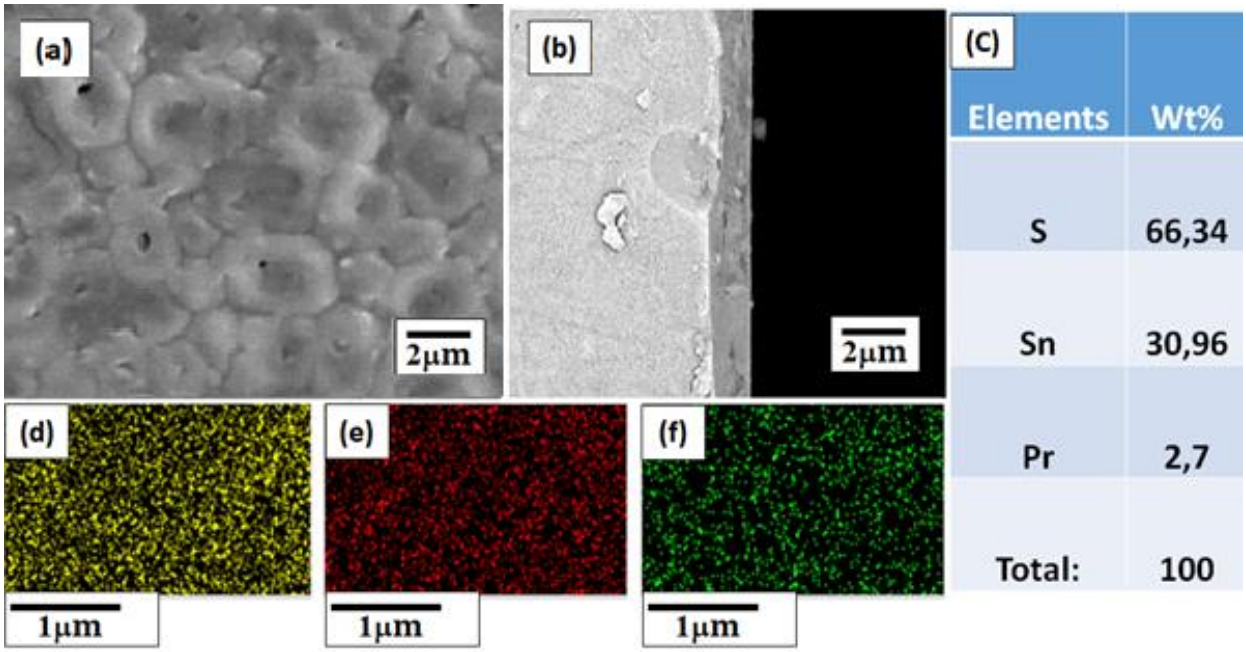

Figure 2. (a) SEM image, **(b)** cross-section image, **(c)** table for the atomic and weight percentage of different elements, and **(d−f)** EDS elemental mapping of 4% Pr-doped SnS_2 materials where; **(d)** Sn, **(e)** S, and **(f)** Pr.

3.4. X-ray photoelectron spectroscopy analysis of SnS_2 and Pr-doped SnS_2 films

XPS was used to analyze the synthesized materials for elemental composition and chemical states. **Figure 3(a)** displays the survey spectra corresponding to the undoped SnS_2 and 4 at % Pr-doped SnS_2 samples, in which the core level photoelectron peaks related to Sn (Sn 3s, 3p, 3d, and 4d), S (S 2s and 2p), and Pr (Pr 3d and 4d) accompanied by Auger transition ones (S LMM, Sn MNN, and Pr MNN) are well identified. Note that the Pr signals only appear in the spectrum of the doped sample. Besides, the presence of adventitious carbon and oxygen in very low signals (O 1s and C 1s) indicates fairly clean surfaces. The atomic percentages of Sn, S, and Pr elements were calculated through the Sn $3d_{5/2}$, S 2p, and Pr $3d_{5/2}$ signals and summarized in the inset table in the same figure. The atomic ratio of [Sn] to [S] is 2.76 for undoped SnS_2 and that of [Sn + Pr] to [S] is 2.81, which is very important compared to the ideal stoichiometric ratio of pure SnS_2 and that derived from EDS results. The significance arises from the fact that XPS can only probe depths of a few nanometers (<10 nm) compared to EDS. Consequently, this observation implies that the surfaces are rich in Sn atoms.

Furthermore, the high-resolution spectra corresponding to Sn 3d, S 2p, and Pr 3d are shown in **Figures 3(b-d)**. The spectra were fitted using Gaussian deconvolution in conjunction with Shirley background subtraction. As shown in **Figure 3(b)**, the doubled Sn 3d spectra indicate that the spin-orbit split of Sn $3d_{5/2}$ -Sn $3d_{3/2}$ main states are 8.40 eV and 8.44 eV for undoped SnS_2 and Pr-doped SnS_2, respectively in agreement with another report [64]. Besides,

for pure SnS_2, only two symmetric peaks of Sn $3d_{5/2}$ -Sn $3d_{3/2}$ states can be found at B.E of 485.97 and 494.37 eV, attributing to the Sn atoms in the Sn^{4+} valence state of Sn-S_2 bonds [9]. However, with the Pr incorporation, these peaks present a shift toward lower binding energies ($\Delta E = 0.47$ eV) accompanied by a little broadening. In addition, two new peaks of Sn $3d_{5/2}$ and Sn $3d_{3/2}$ appeared at higher binding energies (486.5 and 450 eV) and can be referred to as the Sn^{4+} valence state of Sn-O_2 bonds [9]. Similarly, the S 2p region can be deconvoluted into a doublet peak of S $2p_{1/2}$-S $2p_{3/2}$ for pure SnS_2, and two doublets for the doped one, as shown in figure 3(c). The XPS spectrum of Pr 3d doublet peaks (**Figure 3(d)**) are deconvoluted into two doublet peaks located around 933.1 and 928.83 eV. Both doublet peaks belong to the Pr^{+3} chemical state, consistent with the literature [65]. Note that the Pr $3d_{3/2}$ peak is affected by the O KLL peak signals, resulting a peak at around 957.27 eV [62,66,67]. For undoped SnS_2, the peaks of S $2p_{3/2}$ were at 162.3 eV which coincided with those for S^{2-} while for Pr-doped SnS_2, the peaks were located at 162.0 eV (**Figure 3(c)**) [68]. Accordingly, when Sn atoms are replaced by Pr atoms, both Sn 3d and S 2p peaks are shifted toward low binding energies. Based on the findings presented above, it is confirmed that the Pr dopant has been successfully incorporated into the SnS_2 matrix, maintaining a trivalent valence state while acting as a substitute for Sn. This achievement signifies a significant development in altering the material composition, contributing to a deeper understanding of its electronic structure in the context of applications involving photocatalytic degradation and antibacterial activity.

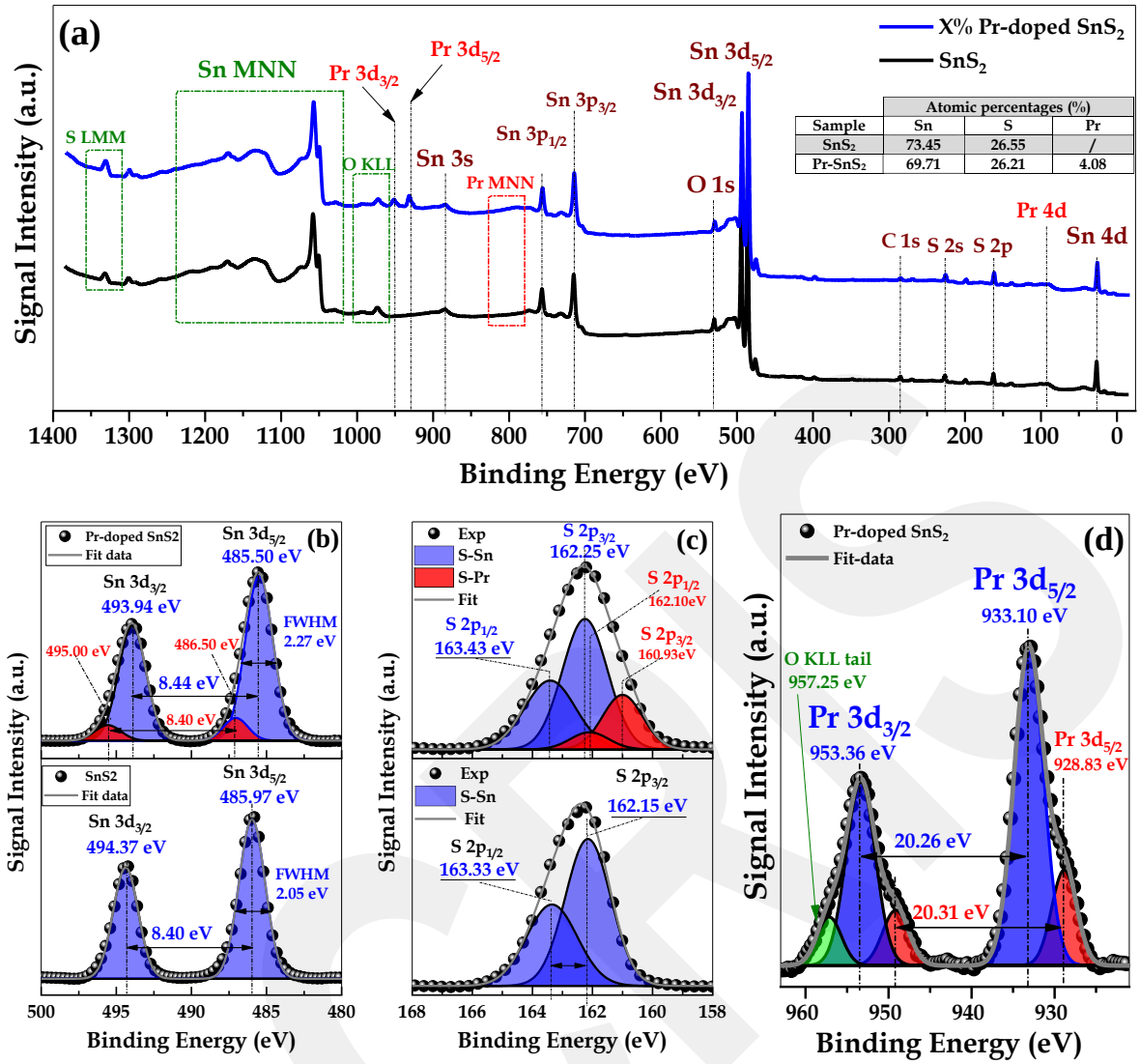

Figure. 3. XPS spectra of undoped SnS_2 and Pr-doped SnS_2; **(a)** Survey scan, **(b)** Sn 3d, **(c)** Pr 3d, **(d)** O 1s, **(e)** S 2p, **(f)** C 1s, and **(g)** fitted XPS of Pr 3d.

3.5. Photocatalytic degradation of Congo red

Photocatalytic degradation of CR was conducted to investigate the photocatalytic activity of SnS_2 synthesized at different temperatures and different percentages of Pr-doped SnS_2 materials under visible light irradiation. Based on **Figure 4(a)** upon the irradiation of visible light, all of the synthesized materials showed degradation of the CR dye which indicates that undoped SnS_2 and Pr-doped SnS_2 exhibited photocatalytic properties. The concentration of the CR dye decreased gradually when undoped SnS_2 was used as a photocatalyst in the degradation. The photocatalytic efficiency of SnS_2 synthesized at 280 °C is much higher in comparison to SnS_2 synthesized at 200 °C with photocatalytic degradation of CR about 50.07% and 40.13 %, respectively. However, when 2% Pr-doped SnS_2 was used as the photocatalyst,

CR dye was degraded more efficiently where it reached 64.06% degradation within 100 min of visible light irradiation. Based on the results obtained, all of the synthesized Pr-doped SnS_2 showed increased photocatalytic performance than undoped SnS_2 and among them, 2% Pr-doped SnS_2 showed outstanding photocatalytic activity under visible light irradiation. This may be attributed to the fact that the doping of Pr into SnS_2 lattice enables the material to harvest visible light more efficiently. Among all the doped thin film, 2% Pr-doped SnS_2 shows highest percentage of degradation due to increased number of charge carriers per particle [69]. Approximately 40.13 %, 50.07 %, 58.26%, and 64.06% CR was degraded by SnS_2 synthesized at 200 °C, SnS_2 synthesized at 280 °C, 4% Pr-doped SnS_2, and 2% Pr-doped SnS_2, respectively. Pr-doped SnS_2 thin film exhibits excellent visible light absorption behaviour, and the optical absorption coefficient in the visible region increases monotonically [70]. Moreover, the photocatalytic degradation activity slowed down at a higher doping percentage (4% Pr-doped SnS_2) [71]. Additionally, the increase in metal dopant concentration creates more electron trap centers [72] and reduces the formation of $^{\bullet}OH$ radicals [73]. The SnS_2 synthesized at 280 °C exhibited superior photocatalytic performance compared to the SnS_2 synthesized at 200 °C. This can be attributed to the prolonged heat treatment of the thick films, which led to the formation of nanocrystals within the inner area of the films [74]. Pr-doped SnS_2 photocatalytic characteristics are contingent upon its crystallinity, shape, size, and exposed facets [75]. Crystallite size and crystallinity have been recognized as important parameters that influence photocatalytic performance [76]. To further delineate the crystalline structure, XRD patterns were employed. The average crystallite sizes, derived from these patterns, were determined to be 59.40 nm for 2% Pr-doped SnS_2, and 65.03 nm for 4% Pr-doped SnS_2. These outcomes provide invaluable insights into the physical characteristics of the photocatalyst, shedding light on both its surface attributes and crystalline structure, crucial for a comprehensive understanding and optimization of its photocatalytic efficacy. The larger crystallite sizes in the doped samples can affect the electronic band structure and surface properties. In photocatalysis, a larger surface area with well-defined crystal facets can provide more active sites for catalytic reactions. In this context, it is reported that higher crystalline quality, characterized by reduced grain boundaries and fewer defects/impurities, enhances the quantum efficiency of particles by minimizing the recombination of photoinduced electron-hole pairs [39]. This, in turn, leads to increased photocatalytic efficiency [59]. As highlighted in the XPS section, Pr doping contributes to heightened crystalline quality and enlarged crystal size, particularly evident at a 4% Pr concentration. Given this information, it is anticipated that 4% Pr-doped SnS_2 should

exhibit superior photocatalytic performance. However, beyond the influence of particle shape, enlarging the particle size to a certain extent can constrain reaction kinetics. Therefore, the superior photocatalytic performance demonstrated by 2% Pr-doped SnS_2 is attributed to its characteristic crystalline structure (size/shape), which facilitates efficient charge transfer and accelerates reaction kinetics [76,77]. It has been pointed out that the energy of photo-generated radicals increases by reducing the crystallite size due to the quantum confinement effect, which improves the performance of the photocatalyst. This effect has been further supported by other authors who have studied various other photocatalytic reactions [78–80]. Additionally, a reduction in the crystallite size leads to larger surface areas thus improving the adsorption of reactants and subsequently enhancing the photo-reactivity [81,82].

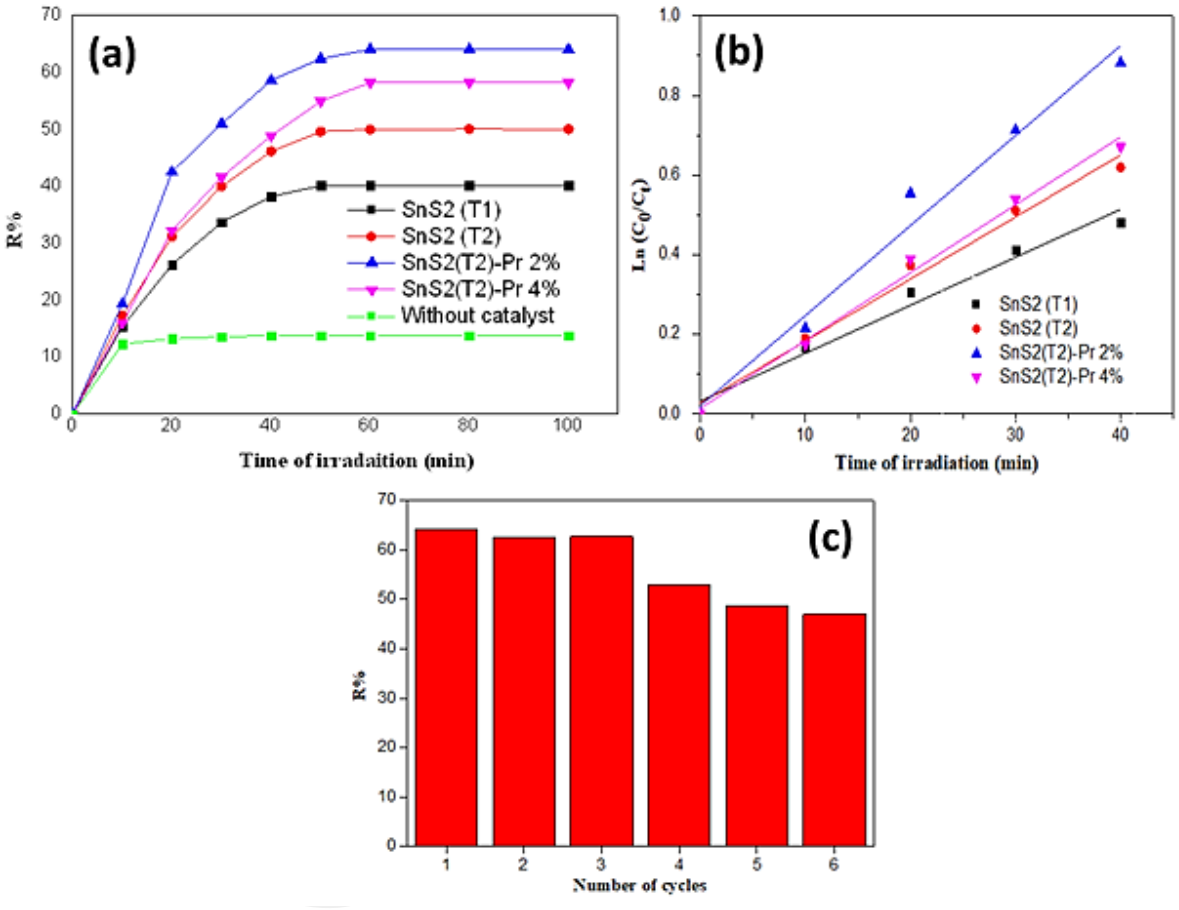

Figure 4. Plot of **(a)** percentage of photocatalytic degradation, **(b)** ln C_0/C_t against time for the photocatalytic degradation of CR using SnS_2 synthesized at 200 and 280 °C and different atomic percentages of Pr-doped SnS_2 thin films, and **(c)** recycling experiments towards CR degradation over 2% Pr-doped SnS_2 thin film.

In a study by Chen and co-workers, they reported heterostructures of Ni-doped SnO_2-SnS_2, denoted as NiSnSO, which were synthesized through the thermal oxidation of Ni-doped SnS_2 [83]. These NiSnSO structures exhibited remarkable catalytic efficiency when employed

for the photocatalytic degradation of organic pollutants. Based on their investigations, the degradation of methyl orange was observed to be 29.8% and 52.1% for pure SnS_2 and Ni-doped SnS_2, respectively prior to the thermal oxidation process. In comparison to their findings, our research shows significant promise and advancement. Indeed, even when more than 30% of the dye remains undegraded, a thin film can still be a highly advantageous material as a photocatalyst. A photocatalyst offers environmental benefits by using light energy to drive reactions. While it may not completely degrade all pollutants, its efficiency, selectivity, and potential for optimization make it a promising tool for pollution remediation.

To gain a better understanding of the photocatalytic degradation of CR, Langmuir-Hinshelwood was used to obtain the kinetic data using the following equations (5)-(9) [84,85]. In this model, the rate of reaction (r) is proportional to the fraction of the surface covered by the CR dye (θ).

$$r = -\frac{dC}{dt} = k\theta \quad \ldots\ldots\ldots\ldots\ldots\ldots\ldots\ldots\ldots\ldots\ldots\ldots\ldots\ldots (5)$$

By that Langmuir's equation into account:

$$\theta = \frac{KC}{(1+KC)} \quad \ldots\ldots\ldots\ldots\ldots\ldots\ldots\ldots\ldots\ldots\ldots\ldots\ldots\ldots (6)$$

$$r = -\frac{dC}{dt} = k\left(\frac{KC}{(1+KC)}\right) \quad \ldots\ldots\ldots\ldots\ldots\ldots\ldots\ldots\ldots\ldots\ldots\ldots\ldots\ldots (7)$$

where 'k' is the true rate constant and 'K' is the constant of the adsorption equilibrium of Langmuir-Hinshelwood. In photocatalytic studies, the value of "K" is determined empirically by a kinetic study in the presence of light and is better than that obtained in the absence of light, starting from Langmuir's isotherm. The concentration of the CR dye at a time "t" is denoted by "C". This equation can be integrated as:

$$\ln\left(\frac{C_0}{C_t}\right) + K(C_0 - C) = kKt \quad \ldots\ldots\ldots\ldots\ldots\ldots\ldots\ldots\ldots\ldots (8)$$

$$r = -\frac{dC}{dt} = kKC = k_{app}C \quad \ldots\ldots\ldots\ldots\ldots\ldots\ldots\ldots\ldots\ldots (9)$$

where C_0 is the initial concentration of CR concentration, C_t is the concentration at t of CR, and k_{app} is the estimated pseudo-first-order rate constant (min^{-1}) derived from the straight lines of the plot $\ln(C_0/C_t)$ versus irradiation time t as shown in **Figure 4(c)**. Thus, equation (9) can be simplified to:

$$\ln\left(\frac{C_0}{C_t}\right) = k_{app}t \quad \ldots\ldots\ldots\ldots\ldots\ldots\ldots\ldots\ldots\ldots\ldots\ldots\ldots (10)$$

The $\ln(C_0/C_t)$ plot vs irradiation time yields the kinetics of the degradation reaction. The "Kapp" represents the slope of the plot. **Figure 4 (b)** shows the rate constant obtained for the synthesized materials whereby 2% Pr-doped SnS_2 exhibited the highest rate constant of 0.02263 ± 0.0018 min^{-1} followed by 4% Pr-doped SnS_2 with rate constant of 0.01706 ± 0.000867 and undoped SnS_2 synthesized at 280 °C with rate constant of 0.01559 ± 0.00104 min^{-1}. While undoped SnS_2 synthesized at 200 °C displayed the lowest rate constant at 0.01207 ± 0.00109 min^{-1}. Moreover, the rate constant of 2% Pr-doped SnS_2 is almost two times faster than undoped SnS_2 as shown in **Table 2**. These results showed that as Pr was introduced into the SnS_2, it significantly enhanced the photocatalytic activity.

Table 2. Pseudo-first-order kinetic parameters of photocatalytic degradation of the CR using pseudo-first order of SnS_2 synthesized at different temperatures and different percentages of Pr-doped SnS_2 thin films.

Parameters of kinetic models	**Undoped SnS_2 (T1)**	**Undoped SnS_2 (T2)**	**2% Pr-doped SnS_2**	**4% Pr-doped SnS_2**
K_{app} (min^{-1})	0.01207 ± 0.00109	0.01559 ± 0.00104	0.02263 ± 0.0018	0.01706 ± 0.000867
R^2	0.96806	0.98253	0.97427	0.98973

In addition, the thin film can be used in multiple cycles, highlighting its potential for efficient and long-term use in pollution remediation operations. For that, multiple cycles of CR photocatalytic degradation were performed on a 2% Pr-doped SnS_2 thin film to study its photocatalytic stability. After each cycle, we discarded the used photocatalyst, cleaned it well in deionized water, and introduced new CR solution (10 mg/L) to the photocatalyst. Each cycle lasted 60 minutes, and six cycles in a row were performed. Despite the fact that the reusability of the 2% Pr-doped SnS_2 thin films was shown to exhibit considerable photocatalytic activity even after 3 cycles of degradation experiments, there were notable changes in the degradation efficiency after more than three reuses as shown in **Figure 4 (c)**. Furthermore, Oluwalana *et al.* improved that the SnS_2 photocatalyst could be reused for four cycles without losing its photodegradation ability [86].

3.6. Photocatalytic antibacterial activity

In this study, the time-kill assay was used to investigate the antibacterial activity of the prepared undoped SnS_2 and Pr-doped SnS_2 thin films against Gram-negative bacteria, *E. coli*. Time-kill curves were generated by plotting $\log_{10}$ CFU/mL against time. The decrease in $\log_{10}$

CFU/mL indicates the bactericidal effect of the synthesized materials. In the time-kill assay, 2% Pr-doped SnS_2 significantly inhibited bacterial growth *of E. coli* when compared with the control, undoped SnS_2, and 4% Pr-doped SnS_2 (**Figure 5(a)**). Based on **Figure 5(b)**, both undoped and Pr-doped SnS_2 showed an increasing trend of reduction of *E. coli* growth as the incubation time increased from 24 to 72 h. The reduction in bacterial growth was <5.5 $\log_{10}$ CFU/mL for 2% Pr-doped SnS_2 which is about 71.03% of *E. coli* dead colonies which is the highest compared to undoped and 4% Pr-doped SnS_2. The 4% Pr-doped SnS_2 showed about 63.29% reduction of *E. coli* while undoped is only about 50.39%. The enhancement in the reduction of *E. coli* growth using 2% Pr-doped SnS_2 may be due to its ability to harvest visible light effectively and produce reactive oxygen species (ROS) that could inhibit the growth of *E. coli*. Previous studies have also shown that visible light irradiation initiates the production of ROS from chalcogenide-based materials [87,88]. These ROS were found to have an antibacterial impact on a variety of bacterial pathogens by causing damage to the cytoplasmic membrane, DNA, cellular oxidation, and lipid peroxidation. Additionally, it was found the crystallite size may also affects the antibacterial activity of the synthesized materials. The higher antibacterial activity of 2% Pr-doped SnS_2 compared to 4% Pr-doped SnS_2 may be due to its smaller crystallite size. This is because smaller-sized particles can effectively interact with bacterial membranes due to their large surface area, thus enhancing their antibacterial efficiency [45].

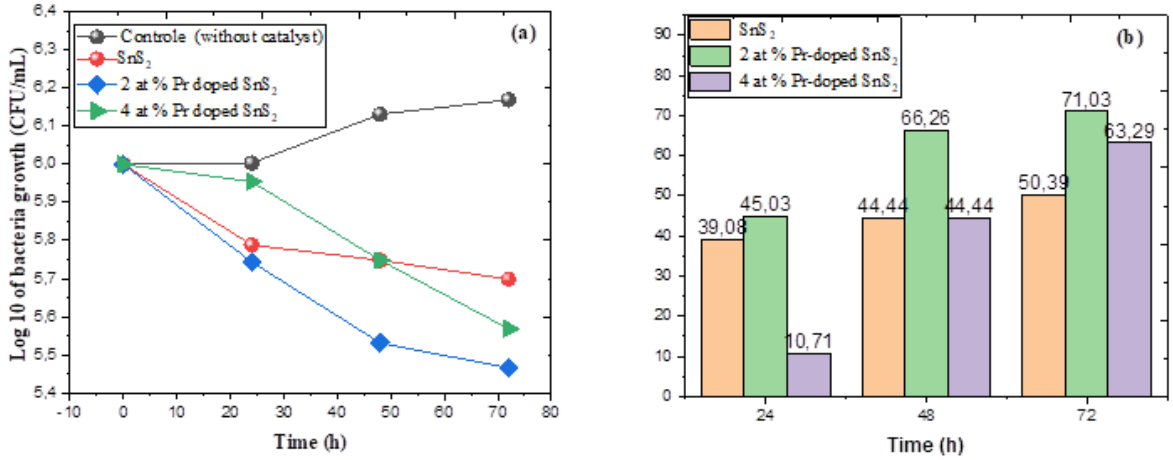

Figure 5. (a) *E. coli* growth in the presence of SnS_2 and Pr-doped SnS_2 thin films over 8 h and **(b)** dead colonies percentage of *E. coli* after exposure to SnS_2 and Pr-doped SnS_2 thin films at different intervals.

4. Conclusion

In this study, a novel approach was employed to synthesize thin films of pure SnS_2 and Pr-doped SnS_2 (2% and 4%) for potential use in photocatalytic degradation and antibacterial applications. This method involved utilizing a spray-coating technique with a transparent molecular ink. This approach stands out due to its cost-effectiveness, simplicity, and rapid deposition characteristics. The utilization of transparent molecular ink introduces innovation to the process, ensuring a uniform and consistent deposition of the thin film. This, in turn, provides better control over the thickness and composition of the film, enhancing its overall performance and applicability for both mentioned applications. XRD, Raman, SEM, and XPS were used to characterize the synthesized SnS_2 and Pr-doped SnS_2 thin films. All of the grown films were pure and exhibited a hexagonal structure, as confirmed by the above-mentioned analysis. Depending on the Pr concentration, the grain size of the films changed. EDX, SEM elemental mapping, and XPS revealed Pr atoms and their uniformity in the SnS_2 film. Moreover, based on XPS results, the majority of the Pr-doping in the SnS_2 matrix is in the trivalent state (Pr^{3+}). Amongst the synthesized thin films, 2% Pr-doped SnS_2 exhibited the highest photocatalytic degradation of CR about 64.06% within 100 min and 71.03% reduction of *E. coli* growth after 72 h. Thus, Pr-doped SnS_2 thin films synthesized via a spray-coated method could prove to be a low-cost sustainable material for the efficient photocatalytic removal of organic dyes such as CR and antibacterial agents against *E. coli*.

5. Acknowledgment

This work is a part of PRFU project N B00L02UN460120220001 supported by Belhadj Bouchaib Ain-Temouchenet University and of Ministry of Research and Innovation, Core Program, Project PN19-35 02 03, Algeria.

6. Declarations Conflict of interest

The authors declare no conflict of interest.

7. References

[1] J.-H. Sun, S.-Y. Dong, J.-L. Feng, X.-J. Yin, X.-C. Zhao, Enhanced sunlight photocatalytic performance of Sn-doped ZnO for Methylene Blue degradation, J Mol Catal A Chem 335 (2011) 145–150. https://doi.org/10.1016/j.molcata.2010.11.026.

[2] V. Vaiano, M. Matarangolo, O. Sacco, D. Sannino, Photocatalytic treatment of aqueous solutions at high dye concentration using praseodymium-doped ZnO catalysts, Appl Catal B 209 (2017) 621–630. https://doi.org/10.1016/j.apcatb.2017.03.015.

[3] A. Khataee, A. Karimi, S. Arefi-Oskoui, R. Darvishi Cheshmeh Soltani, Y. Hanifehpour, B. Soltani, S.W. Joo, Sonochemical synthesis of Pr-doped ZnO nanoparticles for sonocatalytic degradation of Acid Red 17, Ultrason Sonochem 22 (2015) 371–381. https://doi.org/10.1016/j.ultsonch.2014.05.023.

[4] C.B. Ong, L.Y. Ng, A.W. Mohammad, A review of ZnO nanoparticles as solar photocatalysts: Synthesis, mechanisms and applications, Renewable and Sustainable Energy Reviews 81 (2018) 536–551. https://doi.org/10.1016/j.rser.2017.08.020.

[5] V. Vaiano, M. Matarangolo, O. Sacco, D. Sannino, Photocatalytic removal of Eriochrome Black T dye over ZnO nanoparticles doped with Pr, Ce or Eu, Chem Eng Trans 57 (2017) 625–630. https://doi.org/10.3303/CET1757105.

[6] J. Zhang, A. Chen, L. Wang, X. Li, W. Huang, Striving Toward Visible Light Photocatalytic Water Splitting Based on Natural Silicate Clay Mineral: The Interface Modification of Attapulgite at the Atomic-Molecular Level, ACS Sustain Chem Eng 4 (2016) 4601–4607. https://doi.org/10.1021/acssuschemeng.6b00716.

[7] J. Zhang, Q. Wang, L. Wang, X. Li, W. Huang, Layer-controllable WS_2 -reduced graphene oxide hybrid nanosheets with high electrocatalytic activity for hydrogen evolution, Nanoscale 7 (2015) 10391–10397. https://doi.org/10.1039/C5NR01896J.

[8] S. Kant, D. Pathania, P. Singh, P. Dhiman, A. Kumar, Removal of malachite green and methylene blue by Fe0.01Ni0.01Zn0.98O/polyacrylamide nanocomposite using coupled adsorption and photocatalysis, Appl Catal B 147 (2014) 340–352. https://doi.org/10.1016/j.apcatb.2013.09.001.

[9] S. Kannan, N.P. Subiramaniyam, M. Sathishkumar, Effect of annealing temperature and Mn doping on the structural and optical properties of ZnS thin films for enhanced photocatalytic degradation under visible light irradiation, Inorg Chem Commun 119 (2020) 108068. https://doi.org/10.1016/j.inoche.2020.108068.

[10] V. Vatanpour, O. Karatas, S. Amiri, H.R. Rajabi, I. Koyuncu, A. Khataee, Different metal-doped ZnS quantum dots photocatalysts for enhancing the permeability and antifouling performances of polysulfone membranes with and without UV irradiation, Chemosphere 294 (2022) 133705. https://doi.org/10.1016/j.chemosphere.2022.133705.

[11] F. Zhang, Y. Zhang, Y. Wang, A. Zhu, Y. Zhang, Efficient photocatalytic reduction of aqueous Cr (VI) by Zr^{4+} doped and polyaniline coupled SnS_2 nanoflakes, Sep Purif Technol 283 (2022) 120161. https://doi.org/10.1016/j.seppur.2021.120161.

[12] T. Di, T. Cao, H. Liu, S. Wang, J. Zhang, Cu-doped SnS_2 nanosheets with superior visible-light photocatalytic CO_2 reduction performance, Physical Chemistry Chemical Physics 25 (2023) 5196–5202. https://doi.org/10.1039/D2CP04993G.

[13] J. Zou, G. Liao, H. Wang, Y. Ding, P. Wu, J.-P. Hsu, J. Jiang, Controllable interface engineering of g-C_3N_4/CuS nanocomposite photocatalysts, J Alloys Compd 911 (2022) 165020. https://doi.org/10.1016/j.jallcom.2022.165020.

[14] K. Vinotha, B. Jayasutha, M.J. Abel, K. Vinoth, In^{3+}-doped CuS thin films: physicochemical characteristics and photocatalytic property, Journal of Materials

Science: Materials in Electronics 33 (2022) 22862–22882. https://doi.org/10.1007/s10854-022-09056-1.

[15] M. Lal, P. Sharma, C. Ram, Optical, structural properties and photocatalytic potential of Nd-ZnO nanoparticles synthesized by hydrothermal method, Results in Optics 10 (2023) 100371. https://doi.org/10.1016/j.rio.2023.100371.

[16] A.N. Ech-Chergui, A.S. Kadari, M.M. Khan, A. Popad, Y. Khane, M. Guezzoul, C. Leostean, D. Silipas, L. Barbu-Tudoran, Z. Abdelhalim, F. Bennabi, K. Driss-Khodja, B. Amrani, Spray pyrolysis-assisted fabrication of Eu-doped ZnO thin films for antibacterial activities under visible light irradiation, Chemical Papers 77 (2023) 1047–1058. https://doi.org/10.1007/s11696-022-02543-z.

[17] E. Radha, D. Komaraiah, R. Sayanna, J. Sivakumar, Photoluminescence and photocatalytic activity of rare earth ions doped anatase TiO_2 thin films, J Lumin 244 (2022) 118727. https://doi.org/10.1016/j.jlumin.2022.118727.

[18] E. Cerrato, E. Gaggero, P. Calza, M.C. Paganini, The role of Cerium, Europium and Erbium doped TiO_2 photocatalysts in water treatment: A mini-review, Chemical Engineering Journal Advances 10 (2022) 100268. https://doi.org/10.1016/j.ceja.2022.100268.

[19] M.M. Khan, A. Rahman, Chalcogenides and Chalcogenide-Based Heterostructures as Photocatalysts for Water Splitting, Catalysts 12 (2022) 1338. https://doi.org/10.3390/catal12111338.

[20] M.M. Khan, Chalcogenide-Based Nanomaterials as Photocatalysts, Elsevier, 2021. https://doi.org/10.1016/C2019-0-01819-5.

[21] M.M. Khan, S.F. Adil, A. Al-Mayouf, Metal oxides as photocatalysts, Journal of Saudi Chemical Society 19 (2015) 462–464. https://doi.org/10.1016/j.jscs.2015.04.003.

[22] A. Rahman, M.M. Khan, Chalcogenides as photocatalysts, New Journal of Chemistry 45 (2021) 19622–19635. https://doi.org/10.1039/D1NJ04346C.

[23] Mohammad. Mansoob Khan, Theoretical Concepts of Photocatalysis, Elsevier, 2023. https://doi.org/10.1016/C2021-0-01798-3.

[24] S.N. Matussin, A. Rahman, M.M. Khan, Role of Anions in the Synthesis and Crystal Growth of Selected Semiconductors, Front Chem 10 (2022). https://doi.org/10.3389/fchem.2022.881518.

[25] X. Guo, F. Zhang, Y. Zhang, J. Hu, Review on the advancement of SnS_2 in photocatalysis, J Mater Chem A Mater 11 (2023) 7331–7343. https://doi.org/10.1039/D2TA09741A.

[26] A.J. Khimani, S.H. Chaki, R.Kr. Giri, R.R. Meena, R.M. Kannaujiya, M.P. Deshpande, Thermal exploration of sonochemically achieved SnS_2 nanoparticles: Elemental, structural, and morphological investigations of TG residual SnS_2, Chemical Thermodynamics and Thermal Analysis 9 (2023) 100104. https://doi.org/10.1016/j.ctta.2023.100104.

[27] S. Gedi, V.R. Minnam Reddy, T.R.R. Kotte, C. Park, W.K. Kim, Fundamental Aspects and Comprehensive Review on Physical Properties of Chemically Grown Tin-Based Binary Sulfides, Nanomaterials 11 (2021) 1955. https://doi.org/10.3390/nano11081955.

[28] A. Goktas, E. Aslan, F. Arslan, A. Kilic, Characterization of multifunctional solution-processed $Sn_{1-x}Zn_xS$ nanostructured thin films for photosensitivity and photocatalytic applications, Opt Mater (Amst) 133 (2022) 112984. https://doi.org/10.1016/j.optmat.2022.112984.

[29] V. Gadore, S.R. Mishra, M. Ahmaruzzaman, Bio-inspired sustainable synthesis of novel SnS_2/biochar nanocomposite for adsorption coupled photodegradation of amoxicillin and congo red: Effects of reaction parameters, and water matrices, J Environ Manage 334 (2023) 117496. https://doi.org/10.1016/j.jenvman.2023.117496.

[30] P. Ilanchezhiyan, G.M. Kumar, M. Subramanian, R. Jayavel, Effect of Pr doping on the structural and optical properties of ZnO nanorods, Materials Science and Engineering: B 175 (2010) 238–242. https://doi.org/10.1016/j.mseb.2010.07.035.

[31] D. Prabha, S. Ilangovan, S. Balamurugan, M. Suganya, S. Anitha, V.S. Nagarethinam, A.R. Balu, Spectroscopic, magnetic and antibacterial properties of Sr-doped SnS_2 nanopowders, Optik (Stuttg) 142 (2017) 301–310. https://doi.org/10.1016/j.ijleo.2017.06.015.

[32] Z. Yang, S. He, W. Liu, B. Zou, W. Liao, Y. Wang, C. Wang, S. Li, X. Niu, The photocatalytic reduction of U(VI) by Ag-doped SnS_2 materials under visible light, Water Science & Technology 88 (2023) 62–74. https://doi.org/10.2166/wst.2023.210.

[33] C.S. Diko, M. Abitonze, Y. Liu, Y. Zhu, Y. Yang, Synthesis and Applications of Dimensional SnS_2 and SnS_2/Carbon Nanomaterials, Nanomaterials 12 (2022) 4497. https://doi.org/10.3390/nano12244497.

[34] A. Nebatti Ech-Chergui, P.R. Ghediya, Y. Khane, M. Guezzoul, A. Popa, A.S. Kadari, M. Adjdir, K. Kesavan, D.J. Lockwood, K.D. Khodja, B. Amrani, A. Zekri, B. Aïssa, Spray coated of newly La-doped SnS_2 thin films for photocatalytic degradation application, Physica B Condens Matter 667 (2023) 415206. https://doi.org/10.1016/j.physb.2023.415206.

[35] N. Afzali, M. Torka Beydokhti, A.A. Khodadadi, Y. Mortazavi, Tuning the band-gap and enhancing the trichloroethylene photocatalytic degradation activities of flower-like Ni-doped SnS_2/SnO_2heterostructures by partial oxidation, J Environ Chem Eng 10 (2022) 107793. https://doi.org/10.1016/j.jece.2022.107793.

[36] H. Arfin, A.S. Kshirsagar, J. Kaur, B. Mondal, Z. Xia, S. Chakraborty, A. Nag, ns^2 Electron (Bi^{3+} and Sb^{3+}) Doping in Lead-Free Metal Halide Perovskite Derivatives, Chemistry of Materials 32 (2020) 10255–10267. https://doi.org/10.1021/acs.chemmater.0c03394.

[37] Q. Zhang, S. Ma, R. Zhang, K. Zhu, Y. Tie, S. Pei, Optimization NH_3 sensing performance manifested by gas sensor based on Pr-SnS_2/ZnS hierarchical nanoflowers, J Alloys Compd 807 (2019) 151650. https://doi.org/10.1016/j.jallcom.2019.151650.

[38] A.S. Kadari, A.N. Ech-Chergui, B. Aïssa, S.K. Mukherjee, N. Benaioun, Y. Zakaria, A. Zekri, C.M. Reda, A. Mehdi, R. Rabea, K. Driss-Khodja, B. Amrani, Growth and characterization of transparent vanadium doped zinc oxide thin films by means of a spray pyrolysis process for TCO application, J Solgel Sci Technol 103 (2022) 691–703. https://doi.org/10.1007/s10971-022-05875-0.

[39] S. Tair, P.R. Ghediya, A.N. Ech-Chergui, M. Guezzoul, S.K. Mukherjee, K. Driss-Khodja, R. Singh, J. Ray, B. Amrani, n-type SnS_2 thin films spray-coated from transparent molecular ink as a non-toxic buffer layer for solar photovoltaics, Phys Scr 97 (2022) 095810. https://doi.org/10.1088/1402-4896/ac8776.

[40] A. sadek Kadari, A.N. Ech-Chergui, S.K. Mukherjee, L. Velasco, R.K. Singh, M. walid Mohamedi, E. Akyildiz, A. Zoukel, K. Driss-Khodja, B. Amrani, M. Reda Chellali, Atomic mapping of Li:ZnO thin films and its spectroscopic analysis, Inorg Chem Commun 132 (2021) 108852. https://doi.org/10.1016/j.inoche.2021.108852.

[41] A. sadek Kadari, Y. Khane, A. Nebatti Ech-Chergui, A. Popa, M. Guezzoul, D. Silipas, F. Bennabi, A. Zoukel, E. Akyildiz, K. Driss-Khodja, B. Amrani, Growth, properties and photocatalytic degradation of congo red using Gd:ZnO thin films under visible light, Inorg Chem Commun 142 (2022) 109626. https://doi.org/10.1016/j.inoche.2022.109626.

[42] Y. Kim, B. Kaczer, D. Verreck, A. Grill, D. Kim, J. Song, J. Diaz-Fortuny, A. Vici, J. Park, S. Van Beek, M. Simicic, E. Bury, A. Chasin, D. Linten, J. Lee, J. Chun, S. Kim, B. Seo, J. Choi, J.H. Shim, K. Lee, G. Kim, Cyclic Thermal Effects on Devices of Two-Dimensional Layered Semiconducting Materials, Adv Electron Mater 7 (2021) 2100348. https://doi.org/10.1002/aelm.202100348.

[43] D. Burmeister, M.G. Trunk, M.J. Bojdys, Development of metal-free layered semiconductors for 2D organic field-effect transistors, Chem Soc Rev 50 (2021) 11559–11576. https://doi.org/10.1039/D1CS00497B.

[44] S. Mathew, P. Ganguly, S. Rhatigan, V. Kumaravel, C. Byrne, S. Hinder, J. Bartlett, M. Nolan, S. Pillai, Cu-Doped TiO_2: Visible Light Assisted Photocatalytic Antimicrobial Activity, Applied Sciences 8 (2018) 2067. https://doi.org/10.3390/app8112067.

[45] J. Liu, M.D. Rojas-Andrade, G. Chata, Y. Peng, G. Roseman, J.-E. Lu, G.L. Millhauser, C. Saltikov, S. Chen, Photo-enhanced antibacterial activity of ZnO/graphene quantum dot nanocomposites, Nanoscale 10 (2018) 158–166. https://doi.org/10.1039/C7NR07367D.

[46] Y. Liu, Y. Zhou, X. Zhou, X. Jin, B. Li, J. Liu, G. Chen, Cu doped SnS_2 nanostructure induced sulfur vacancy towards boosted photocatalytic hydrogen evolution, Chemical Engineering Journal 407 (2021) 127180. https://doi.org/10.1016/j.cej.2020.127180.

[47] F. Aslan, F. Arslan, A. Tumbul, A. Goktas, Synthesis and characterization of solution processed p-SnS and n-SnS_2 thin films: Effect of starting chemicals, Opt Mater (Amst) 127 (2022). https://doi.org/10.1016/j.optmat.2022.112270.

[48] I.B. Kherchachi, H. Saidi, A. Attaf, N. Attaf, A. bouhdjar, H. bendjdidi, youcef Benkhetta, R. Azizi, M. Jlassi, Influence of solution flow rate on the properties of SnS_2

films prepared by ultrasonic spray, Optik (Stuttg) 127 (2016) 4043–4046. https://doi.org/10.1016/j.ijleo.2016.01.120.

[49] L. Amalraj, C. Sanjeeviraja, M. Jayachandran, Spray pyrolysised tin disulphide thin film and characterisation, J Cryst Growth 234 (2002) 683–689. https://doi.org/10.1016/S0022-0248(01)01756-0.

[50] C. Khélia, K. Boubaker, T. Ben Nasrallah, M. Amlouk, S. Belgacem, Morphological and thermal properties of β-SnS_2 sprayed thin films using Boubaker polynomials expansion, J Alloys Compd 477 (2009) 461–467. https://doi.org/10.1016/j.jallcom.2008.10.051.

[51] K.T. Ramakrishna Reddy, P. Purandar Reddy, R.W. Miles, P.K. Datta, Investigations on SnS films deposited by spray pyrolysis, Opt Mater (Amst) 17 (2001) 295–298. https://doi.org/10.1016/S0925-3467(01)00052-0.

[52] K. Paulraj, S. Ramaswamy, I.S. Yahia, A.M. Alshehri, H.H. Somaily, H.-S. Kim, A. Kathalingam, Praseodymium doped PbS thin films for optoelectronic applications prepared by nebulizer spray pyrolysis, Applied Physics A 126 (2020) 503. https://doi.org/10.1007/s00339-020-03686-0.

[53] A.G. Manohari, S. Dhanapandian, C. Manoharan, K.S. Kumar, T. Mahalingam, Effect of doping concentration on the properties of bismuth doped tin sulfide thin films prepared by spray pyrolysis, Mater Sci Semicond Process 17 (2014) 138–142. https://doi.org/10.1016/j.mssp.2013.09.012.

[54] Z. Aba, A. Goktas, A. Kilic, Characterization of $Zn_{1-x}La_xS$ thin films; compositional, surface, optical, and photoluminescence properties for possible optoelectronic and photocatalytic applications, J Solgel Sci Technol 109 (2024) 260–271. https://doi.org/10.1007/s10971-023-06273-w.

[55] V. Mote, Y. Purushotham, B. Dole, Williamson-Hall analysis in estimation of lattice strain in nanometer-sized ZnO particles, Journal of Theoretical and Applied Physics 6 (2012) 6. https://doi.org/10.1186/2251-7235-6-6.

[56] A.O. Bokuniaeva, A.S. Vorokh, Estimation of particle size using the Debye equation and the Scherrer formula for polyphasic TiO_2 powder, J Phys Conf Ser 1410 (2019) 012057. https://doi.org/10.1088/1742-6596/1410/1/012057.

[57] G.K. Williamson, R.E. Smallman, III. Dislocation densities in some annealed and cold-worked metals from measurements on the X-ray debye-scherrer spectrum, Philosophical Magazine 1 (1956) 34–46. https://doi.org/10.1080/14786435608238074.

[58] A.G. Manohari, S. Dhanapandian, C. Manoharan, K.S. Kumar, T. Mahalingam, Effect of doping concentration on the properties of bismuth doped tin sulfide thin films prepared by spray pyrolysis, Mater Sci Semicond Process 17 (2014) 138–142. https://doi.org/10.1016/j.mssp.2013.09.012.

[59] M. Abdelkrim, M. Guezzoul, M. Bedrouni, M. Bouslama, A. Ouerdane, B. Kharroubi, Effect of slight cobalt incorporation on the chemical, structural, morphological,

optoelectronic, and photocatalytic properties of ZnO thin film, J Alloys Compd 920 (2022) 165703. https://doi.org/10.1016/j.jallcom.2022.165703.

[60] Y. Ding, W. Zheng, X. Lu, Y. Liang, Y. Zhu, M. Jin, F. Huang, Raman Tensor of Layered SnS_2, J Phys Chem Lett 11 (2020) 10094–10099. https://doi.org/10.1021/acs.jpclett.0c03024.

[61] C. Gurnani, S.L. Hawken, A.L. Hector, R. Huang, M. Jura, W. Levason, J. Perkins, G. Reid, G.B.G. Stenning, Tin(<scp>iv</scp>) chalcogenoether complexes as single source precursors for the chemical vapour deposition of SnE_2 and SnE (E = S, Se) thin films, Dalton Transactions 47 (2018) 2628–2637. https://doi.org/10.1039/C7DT03848H.

[62] V. Natarajan, M. Ahmad, J. Paul Sharma, A. Sathya, P. Kumar Sharma, R. Thangaraj, Interfacial charge-transfer for robust Raman quenching in staggered band aligned n-SnS_2/p-rGO heterostructures, Appl Surf Sci 550 (2021) 149356. https://doi.org/10.1016/j.apsusc.2021.149356.

[63] L.H. Hoang, N.T.M. Hien, N.H. Hai, P. Van Hai, N.T. Khoi, I.-S. Yang, Raman spectroscopy of Cu doping in $Zn_{1-x}Co_xO$ diluted magnetic semiconductor, Journal of Raman Spectroscopy 40 (2009) 1535–1538. https://doi.org/10.1002/jrs.2295.

[64] W. Ren, J. Yang, W. Chen, J. Zhang, Y. Sun, Y. Zheng, H. Zhao, B. Liang, In situ synthesis of novel 0D/ 2D SnO_2 nanoparticles/ SnS_2 nanosheets S-scheme heterojunction for enhancing the photocatalytic pollutant degradation, Mater Res Bull 153 (2022). https://doi.org/10.1016/j.materresbull.2022.111884.

[65] J.-S. Kim, C.W. Na, C.-H. Kwak, H.-Y. Li, J.W. Yoon, J.-H. Kim, S.-Y. Jeong, J.-H. Lee, Humidity-Independent Gas Sensors Using Pr-Doped In_2O_3 Macroporous Spheres: Role of Cyclic Pr^{3+}/Pr^{4+} Redox Reactions in Suppression of Water-Poisoning Effect, ACS Appl Mater Interfaces 11 (2019) 25322–25329. https://doi.org/10.1021/acsami.9b06386.

[66] A.V. Shlyakhtina, J.C.C. Abrantes, E. Gomes, A.N. Shchegolikhin, G.A. Vorobieva, K.I. Maslakov, A.V. Knotko, L.G. Shcherbakova, Effect of Pr3+/Pr4+ ratio on the oxygen ion transport and thermomechanical properties of the pyrochlore and fluorite phases in the ZrO_2–Pr_2O_3 system, Int J Hydrogen Energy 41 (2016) 9982–9992. https://doi.org/10.1016/j.ijhydene.2016.02.152.

[67] J.F. Moulder, Jill. Chastain, Handbook of x-ray photoelectron spectroscopy : a reference book of standard spectra for identification and interpretation of XPS data, Physical Electronics Division, Perkin-Elmer Corp, 1992.

[68] W. Zhao, M. He, F. Chen, X. Jin, H. Duan, M. Long, Z. Wu, B. Cao, Y. Yu, One-pot synthesis of flower-like SnS_2/SnO_2 heterojunction with enhanced visible light photocatalytic performance, Opt Mater (Amst) 123 (2022). https://doi.org/10.1016/j.optmat.2021.111934.

[69] D. Kapusuz, J. PARK, A. Öztürk, INFLUENCE OF BORON AND/OR ZIRCONIUM DOPING ON MORPHOLOGY AND OPTICAL PROPERTIES OF TITANIA, 3rd

International Conference on NANOCON (2011). https://open.metu.edu.tr/handle/11511/55864 (accessed January 2, 2024).

[70] F.F. Xia, F.L. Yang, J. Hu, C.Z. Zheng, H.B. Yi, J.H. Sun, Enhanced visible light absorption performance of SnS_2 and $SnSe_2$ *via* surface charge transfer doping, RSC Adv 8 (2018) 40464–40470. https://doi.org/10.1039/C8RA08834A.

[71] R.K. Mulpuri, S.R. Tirukkovalluri, M.R. Imandi, S.A. Alim, V.D.L. Kapuganti, Zinc and boron co-doped nanotitania with enhanced photocatalytic degradation of Acid Red 6A under visible light irradiation, Sustainable Environment Research 29 (2019) 29. https://doi.org/10.1186/s42834-019-0031-6.

[72] H. Lachheb, E. Puzenat, A. Houas, M. Ksibi, E. Elaloui, C. Guillard, J.-M. Herrmann, Photocatalytic degradation of various types of dyes (Alizarin S, Crocein Orange G, Methyl Red, Congo Red, Methylene Blue) in water by UV-irradiated titania, Appl Catal B 39 (2002) 75–90. https://doi.org/10.1016/S0926-3373(02)00078-4.

[73] C. Ooka, H. Yoshida, M. Horio, K. Suzuki, T. Hattori, Adsorptive and photocatalytic performance of TiO_2 pillared montmorillonite in degradation of endocrine disruptors having different hydrophobicity, Appl Catal B 41 (2003) 313–321. https://doi.org/10.1016/S0926-3373(02)00169-8.

[74] J. Yu, X. Zhao, Q. Zhao, Effect of film thickness on the grain size and photocatalytic activity of the sol-gel derived nanometer TiO_2 thin films, n.d. https://doi.org/https://doi.org/10.1023/A:1006705316651.

[75] O. CARP, Photoinduced reactivity of titanium dioxide, Progress in Solid State Chemistry 32 (2004) 33–177. https://doi.org/10.1016/j.progsolidstchem.2004.08.001.

[76] X. Wang, L. Sø, R. Su, S. Wendt, P. Hald, A. Mamakhel, C. Yang, Y. Huang, B.B. Iversen, F. Besenbacher, The influence of crystallite size and crystallinity of anatase nanoparticles on the photo-degradation of phenol, J Catal 310 (2014) 100–108. https://doi.org/10.1016/j.jcat.2013.04.022.

[77] K.Y. Jung, S. Bin Park, S.-K. Ihm, Linear relationship between the crystallite size and the photoactivity of non-porous titania ranging from nanometer to micrometer size, Appl Catal A Gen 224 (2002) 229–237. https://doi.org/10.1016/S0926-860X(01)00784-0.

[78] M.R. Hoffmann, S.T. Martin, W. Choi, D.W. Bahnemann, Environmental Applications of Semiconductor Photocatalysis, Chem Rev 95 (1995) 69–96. https://doi.org/10.1021/cr00033a004.

[79] J. Jiu, F. Wang, M. Adachi, Preparation of highly photocatalytic active nano-scale TiO_2 by mixed template method, Mater Lett 58 (2004) 3915–3919. https://doi.org/10.1016/j.matlet.2004.08.017.

[80] K.L. Yeung, A.J. Maira, J. Stolz, E. Hung, N. Ka-Chun Ho, A.C. Wei, J. Soria, K.-J. Chao, P.L. Yue, Ensemble Effects in Nanostructured TiO_2 Used in the Gas-Phase Photooxidation of Trichloroethylene, J Phys Chem B 106 (2002) 4608–4616. https://doi.org/10.1021/jp0131121.

[81] M. Xie, L. Jing, J. Zhou, J. Lin, H. Fu, Synthesis of nanocrystalline anatase TiO_2 by one-pot two-phase separated hydrolysis-solvothermal processes and its high activity for photocatalytic degradation of rhodamine B, J Hazard Mater 176 (2010) 139–145. https://doi.org/10.1016/j.jhazmat.2009.11.008.

[82] N. Xu, Z. Shi, Y. Fan, J. Dong, J. Shi, M.Z.-C. Hu, Effects of Particle Size of TiO_2 on Photocatalytic Degradation of Methylene Blue in Aqueous Suspensions, Ind Eng Chem Res 38 (1999) 373–379. https://doi.org/10.1021/ie980378u.

[83] D. Chen, S. Huang, R. Huang, Q. Zhang, T.-T. Le, E. Cheng, R. Yue, Z. Hu, Z. Chen, Construction of Ni-doped SnO_2-SnS_2 heterojunctions with synergistic effect for enhanced photodegradation activity, J Hazard Mater 368 (2019) 204–213. https://doi.org/10.1016/j.jhazmat.2019.01.009.

[84] D. Aouf, A. Henni, D. Selloum, Y. Khane, F. Fenniche, D. Zerrouki, H. Belkhalfa, N. Dizge, Facile preparation and characterization of nanostructured ZnS/PbS heterojunction thin films for enhanced microbial inhibition and photocatalytic degradation, Mater Chem Phys 295 (2023) 127059. https://doi.org/10.1016/j.matchemphys.2022.127059.

[85] A. Abboudi, S. Iaiche, A. Djelloul, A. Chala, F. Kezzoula, F. Bensouici, M. Bououdina, M. Humayun, Effect of fluoric acid concentration on the structural, optical, and photocatalytic properties of TiO_2 thin films, Inorg Chem Commun 155 (2023) 111073. https://doi.org/10.1016/j.inoche.2023.111073.

[86] A.E. Oluwalana, P.A. Ajibade, Preparation and morphological studies of tin sulfide nanoparticles and use as efficient photocatalysts for the degradation of rhodamine B and phenol, Nanotechnol Rev 11 (2022) 883–896. https://doi.org/10.1515/ntrev-2022-0054.

[87] L. Chen, M.-L. Tsai, Y. Chuang, C.-W. Chen, C.-D. Dong, Construction of carbon nanotubes bridged MoS_2/ZnO Z-scheme nanohybrid towards enhanced visible light driven photocatalytic water disinfection and antibacterial activity, Carbon N Y 196 (2022) 877–889. https://doi.org/10.1016/j.carbon.2022.05.055.

[88] M.K. Okla, B. Janani, A.A. AL-ghamdi, M.A. Abdel-Maksoud, H. AbdElgawad, A. Das, S.S. Khan, Facile construction of 3D CdS-Ag_2S nanospheres: a combined study of visible light responsive phtotocatalysis, antibacterial and anti-biofilm activity, Colloids Surf A Physicochem Eng Asp 632 (2022) 127729. https://doi.org/10.1016/j.colsurfa.2021.127729.